SCIENCE CHINA
Chemistry

•ARTICLES•

https://doi.org/10.1007/s11426-022-1264-y

Lowing the energy loss of organic solar cells by molecular packing engineering *via* multiple molecular conjugation extension

Hongbin Chen[1†], Yalu Zou[1†], Huazhe Liang[1], Tengfei He[1,2], Xiaoyun Xu[3], Yunxin Zhang[2], Zaifei Ma[3], Jing Wang[4], Mingtao Zhang[1], Quanwen Li[2], Chenxi Li[1], Guankui Long[2*], Xiangjian Wan[1], Zhaoyang Yao[1*] & Yongsheng Chen[1*]

[1]*State Key Laboratory and Institute of Elemento-Organic Chemistry, Centre of Nanoscale Science and Technology and Key Laboratory of Functional Polymer Materials, Renewable Energy Conversion and Storage Center (RECAST), College of Chemistry, Nankai University, Tianjin 300071, China;*

[2]*School of Materials Science and Engineering, National Institute for Advanced Materials, Renewable Energy Conversion and Storage Center (RECAST), Nankai University, Tianjin 300350, China;*

[3]*State Key Laboratory for Modification of Chemical Fibers and Polymer Materials, Center for Advanced Low-dimension Materials, College of Materials Science and Engineering, Donghua University, Shanghai 201620, China;*

[4]*School of Materials Science & Engineering, Tianjin University of Technology, Tianjin 300384, China*

Received April 25, 2022; accepted April 26, 2022; published online May 6, 2022

The central unit (benzo[*c*][1,2,5]thiadiazole) in **Y6** series of molecules plays a determining role in their unique intermolecular packing for a three-dimensionally (3D) network, largely endowing their organic solar cells (OSCs) with so far the best power conversion efficiencies (PCEs) and also largely suppressed energy losses (E_{loss}). Despite its vital role in molecular packing, very few explorations for central unit have been conducted due to possibly the constructing challenge of central heterocyclic units. Herein, a highly efficient acceptor-donor-acceptor (A-D-A) type electron acceptor, **CH17**, has been designed and constructed, featured with a prominent π extension in both directions of the central and end units with respect to **Y6** series. Such a multiple and much enhanced conjugation extension in **CH17** enables a much more effective and compact 3D molecular packing compared with that of **Y6** supported by X-ray single crystal and other analysis, mainly caused by a newly observed distinctive dual "end unit to central unit" packing mode. This much favorable molecular packing, also kept in its blends with donor materials, leads a larger electron and hole transfer integrals and hence much improved charge transport, and reduced energetic disorders in **CH17** blends. More importantly, the observed upshifted charge transfer (CT) state of **CH17** blends compared with that of **Y6**, due to its increased molecular conjugation extension in both directions, further enhances the hybridization between its CT and local exciton (LE) states, resulting in higher luminescence efficiency, much suppressed non-radiative recombination loss and smaller E_{loss} with respect to that of **Y6**. Consequently, an excellent PCE of 17.84% is achieved with **PM6** as the donor in a binary device compared with a PCE of 16.27% for the controlled **Y6** device. Furthermore, a further improved PCE of 18.13% is achieved by **CH17**-based ternary single-junction OSCs along with a markedly reduced E_{loss} of 0.49 eV and larger open-circuit voltage (V_{oc}) of 0.89 V, compared with that (16.27% of PCE, 0.85 V of V_{oc}, and 0.53 eV of E_{loss}) of the control device using **Y6**. This significantly improved photovoltaic performance caused by molecular multiple conjugation extension, especially through the largely unexplored central unit, indicates that there is still much room to further enhance OSC performance by addressing the most important issue for OSC, *i.e*, the smaller V_{oc} caused by larger E_{loss}, through engineering molecular packing by designing/tuning molecule more dedicatedly.

†These authors contributed equally to this work.
*Corresponding authors (email: yschen99@nankai.edu.cn; zyao@nankai.edu.cn; longgk09@nankai.edu.cn)

organic solar cells, A-D-A electron acceptor, reduced E_{loss}, central unit, multiple conjugation extension, molecular packing

Citation: Chen H, Zou Y, Liang H, He T, Xu X, Zhang Y, Ma Z, Wang J, Zhang M, Li Q, Li C, Long G, Wan X, Yao Z, Chen Y. Lowing the energy loss of organic solar cells by molecular packing engineering *via* multiple molecular conjugation extension. *Sci China Chem*, 2022, 65, https://doi.org/10.1007/s11426-022-1264-y

1 Introduction

With the intrinsic merits of low cost, tunable transparency and color, flexibility, nontoxicity and lightweight, organic solar cells (OSCs) have been regarded as a promising photon-to-current conversion technology in the last few decades [1–5]. The active layer of OSCs is usually composed of an electron donor (D) and acceptor (A) pair, which plays a dominant role in achieving high power conversion efficiencies (PCEs). Among them, the recently developed non-fullerene acceptors (NFAs) with an acceptor-donor-acceptor (A-D-A) architecture have attracted extensive attention due to their distinctive advantages of superior charge separation and transport features mainly caused by their unique frontier electron density distributions [6,7], and over 18% PCEs have been achieved [8–10]. However, despite the markedly increasing PCEs, OSCs still lag far behind that of silicon and perovskite solar cells (PSCs) with common efficiencies over 20% [11,12]. Note that comparable short current densities (J_{sc}) of ~26 mA cm^{-2} and fill factors (FFs) of ~80% have been achieved by OSCs [9,10], whereas the open-circuit voltage (V_{oc}) is still significantly lower than PSCs with similar optical bandgaps [13]. The inferior V_{oc} of OSCs is mostly caused by the significantly larger energy losses (E_{loss}) of 0.5–0.6 eV [13–15], much higher than that of 0.3–0.4 eV for crystalline silicon and PSCs [12,16]. For example, by reducing the E_{loss} of state-of-the-art OSCs to the similar values of PSCs, such as 0.4 eV or less, over 20% PCEs could be achieved immediately based on our semi empirical model [7,17]. Thus, the last and probably also the most important challenge confronted by OSCs currently is to achieve similar V_{oc} to that of inorganic solar cells by suppressing E_{loss}, if similar or even better PCEs should be achieved. Unfortunately, while significant progress has been made [18–23], it is still not fully understood for the complicated determining mechanism and multiple tangling factors related to E_{loss}.

Above the general requirements at the molecular levels, such as ideal absorption and suitable frontier molecular orbital energy levels, it has been largely understood at the morphology level that an optimal and nanoscale intermolecular penetrating network between donor and acceptor in the bulk-heterojunction active layer, preferably with three-dimensionally (3D) network for both D and A molecules, is indispensable for high performance of OSCs. The significance of such ideal morphology requirement has been demonstrated in many studies [24–26], but probably best for the **Y6** systems [9,18,27–30]. With respect to some other NFAs like **ITIC** [31,32] and **F** [33,34] analogs with mainly "end unit to end unit" ("E/E" mode, see discussion below) intermolecular packing, one unique characteristic that contributes most to the high PCEs of **Y6**-based OSCs should be that the central unit (benzo[c][1,2,5]thiadiazole) is strongly involved in the intermolecular packing, and of which most importantly leads to an effective nanoscale 3D network among the acceptor molecules [21,35]. Clearly, this can boost efficient charge separation/transfer/transport and also suppress geminate recombination significantly in blend films, thereby contributing most to the top PCE with relatively smaller E_{loss} at ~0.53 eV for their OSCs [9,27,36]. Therefore, using the original **Y6** molecule as the starting point [27], its various chemical modifications of (1) side chains, (2) bridging thieno [3,2-*b*] thiophenes unit, and (3) end units have been implemented (Figure 1a) [5,9,18,36–48], rendering the continuously improved PCEs and reduced E_{loss} for **Y6** series molecules. Surprisingly, however, among all the **Y6** varieties only a very few adopted an optimized central unit [49,50]. This is even more puzzled if notice that the unique central unit in **Y6** molecule is playing a dominating role in the existing unique 3D packing mode in the active layer, as mentioned above [21,35]. Note such a unique 3D packing network is believed to be the main driving force for its superior performance compared with other A-D-A acceptors, which has been studied and proven by many excellent studies very recently [9,21,35,38].

With these thoughts, we believe it is quite meaningful and also probably challenging to design and construct some molecules using the original **Y6** as the backbone, but with more optimization in both the directions of central and end units to further optimize/strengthen its unique 3D packing network, leading to a smaller E_{loss} and thus higher PCEs. Therefore, a new A-D-A type acceptor **CH17** (Figure 1a) has been designed and synthesized by extending both the central unit and end unit 2-(6,7-difluoro-3-oxo-2,3-dihydro-1*H*-cyclopenta[*b*]naphthalen-1-ylidene) malononitrile (**NINCN-2F**) [51,52]. **CH17**, with two-direction extended conjugation, possesses rather similar the highest occupied orbitals (HOMO), the lowest unoccupied molecular orbital (LUMO), band gap, and film absorption compared with those of **Y6**. But importantly, such a multiple and significantly enhanced conjugation extension of **CH17** boosts effectively the 3D molecular arrangement and also improves

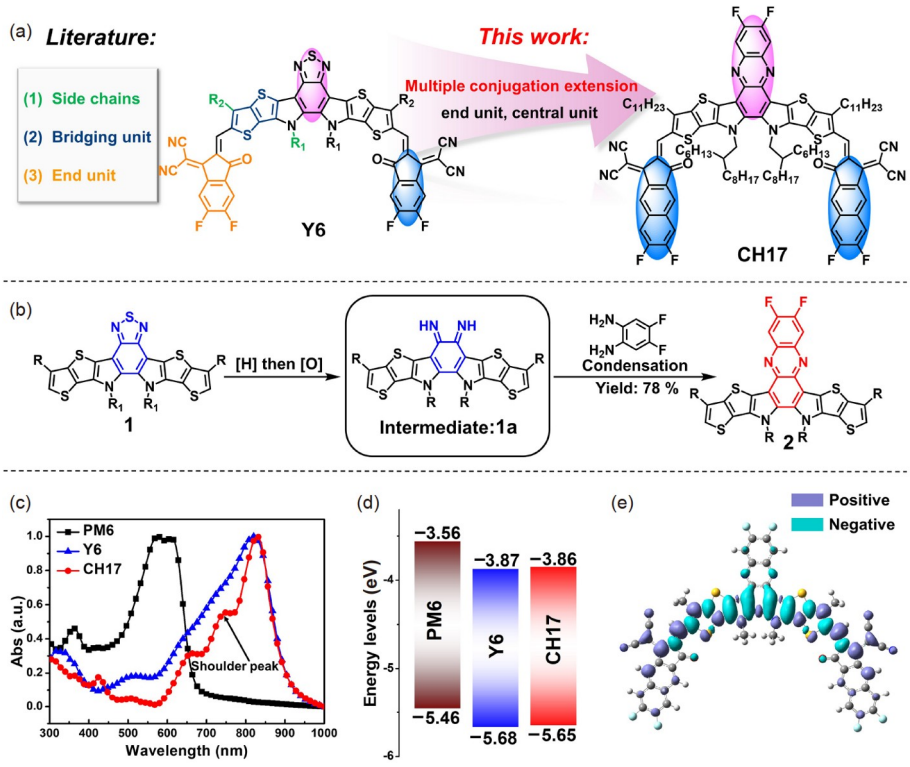

Figure 1 Molecular structures and photophysical properties. (a) Various chemical modifications of **Y6** ((1) side chains, (2) bridging thieno [3,2-*b*] thiophenes unit, and (3) end units)) in previous Refs. [5,9,18,36–48] and molecular structure of **CH17** by multiple conjugation extension optimization (central and end units) in this work. (b) Synthesis route to the key central unit of **CH17**. [H] and [O] represent reduction and oxidation, respectively. (c) Normalized absorption spectra of **PM6**, **Y6**, and **CH17** films. (d) Energy levels diagram of **PM6**, **Y6**, and **CH17**. (e) Iso-surface of charge density difference (ΔQ) for **CH17**, where $\Delta Q=\Psi^2_{\mathrm{LUMO}}-\Psi^2_{\mathrm{HOMO}}$. The positive and negative parts with different colors refer to $\Delta Q>0$ and $\Delta Q<0$, respectively [7] (color online).

its ambipolar charge transport property compared with that of **Y6**, mainly enabled by a newly observed distinctive dual "end unit to central unit" packing mode ("dual E/C" mode). This more favorable molecular packing leads to a bundle-like nanofiber morphology in **CH17** blends with a lower Urbach energy (E_u) and also enhances the hybridization between its charge transfer (CT) and local exciton (LE) states of **CH17**, resulting in higher luminescence efficiency of CT state and suppressed non-radiative recombination loss with respect to that of **Y6**. As a result, an excellent PCE of 18.13% is achieved by **CH17**-based ternary OSCs with **PM6** [53] as the donor, compared with 16.27% of the control device when the original **Y6** was used with the same donor molecule. Importantly, this comes along with a surprisingly larger V_{oc} of 0.89 V and markedly reduced E_{loss} of 0.49 eV compared with 0.85 V of V_{oc} and 0.53 eV of E_{loss} for the controlled **Y6** device (note **CH17** has a quite similar HOMO/LUMO and absorption band gap with **Y6**). These results are consistent with the improved electron and hole transfer integrals and hence improved charge transport based on its single crystal data analysis and theoretical calculation. All of these could be addressed on the unique and strong intermolecular packing of "dual E/C" mode caused by the multiple molecular conjugation extension. The smaller E_{loss} and larger V_{oc} of **CH17** based OSCs make us believe that it should still have huge potential to further engineer the 3D morphology packing, particularly through the central unit conjugation expansion to address the relatively larger E_{loss} issue and smaller V_{oc} of OSC and achieve even higher performance for this emerging solar cell platform.

2 Results and discussion

2.1 Synthesis and characterization

The successfully synthesized route to **CH17** was displayed in Scheme S1 (Supprorting Information online) and the detailed procedures and characterizations were described in Schemes S2–S4. Note both the end and central units of **CH17** are F-substituted for two reasons: (1) F atoms on the end unit are to be consistent with that of **Y6**; (2) hopefully these F atoms would further enhance the intermolecular interaction [38]. Therefore, **CH17** has been synthesized in a four-step route with the indispensable but challenging step of phenazine conversion from benzothiadiazole. As shown in Figure 1b, an *in-situ* reaction to afford the central donor (**2**) in a good yield was developed by converting compound **1** into an intermediate diimine (**1a**) firstly by reduction and

subsequent oxidation, and further followed by an *in-situ* condensation with commercially available 4,5-difluoro-1,2-phenylenediamine. This *in-situ* but necessary transformation might partially explain the much unexplored variety of **Y6** with central unit modification, which would be an effective and convenient method for future central unit modification of **Y6** series of molecules. Note that the multiple conjugated extension of backbone of **CH17** may cause low solubility with respect to **Y6**, thereby the elongation of alkyl chains on sp^2 N atoms becomes necessary to ensure its good solubility in commonly used solvents including chloroform, toluene, 1-chloronaphthalene, and chlorobenzene.

Figure 1c and Figure S1 (Supprorting Information online) show and compare the normalized absorption spectra of **CH17** and **Y6** in neat films and solutions, respectively. In dilute chloroform solutions (Figure S1), **CH17** possesses a bathochromically shifted maximum absorption wavelength (λ_{max}) of 773 nm and also enhanced molar extinction coefficient of 2.31×10^5 M^{-1} cm^{-1} with respect to those of **Y6** (732 nm and 1.86×10^5 M^{-1} cm^{-1}, respectively). At solid state shown in Figure 1c, **CH17** displays a much clearer shoulder peak at a lower wavelength of 750 nm compared with that of **Y6**, suggesting an effective intermolecular π-π stacking for **CH17** [38]. Note both the λ_{max} of 822 nm and onset absorption (E_g^{onset}) of 914 nm for **CH17** film are very close to those of **Y6** (820 and 911 nm, respectively). These absorption data clearly indicate that the designed multiple conjugation extension leads **CH17** with an enhanced molecular stacking and light harvesting compared with that of **Y6**. Then the cyclic voltammetry (CV) was performed to evaluate the energy levels of **CH17** and **Y6** side-by-side for an accurate comparison (Figures S2 and S3). As shown in Figure 1d, very similar HOMOs and LUMOs can be observed for **CH17** and **Y6**. Note that the relative alignment of energy levels derived from CVs is in accordance with the results from theoretical calculations (Figure S5). Furthermore, thermal gravimetric analysis (TGA) was applied to evaluate the thermal stability of NFAs (Figure S4), both showing excellent thermal stability with a decomposition temperature of ~336 °C for **CH17** and ~329 °C for **Y6**, respectively. The detailed parameters of physicochemical properties for **CH17** and **Y6** were summarized in Table S1 (Supprorting Information online) for a clear comparison. In addition, the clear A-D-A feature of **CH17** is demonstrated by its characteristic peak-valley-peak plot along the longest direction of molecular backbone (Figure 1e and Figure S6) for its frontier orbital charge density difference (ΔQ) [7]. As it has been proposed before, such a unique feature with a peak-valley-peak plot of ΔQ for A-D-A type molecules would endow enhanced molar extinction coefficient, better exciton separation and charge transportation, smaller energy losses, and thus leading a better performance of OSCs compared with other types of moelcules [7].

2.2 Molecular packing in CH17 single crystal

As we mentioned above, **CH17** was designed to better engineer the unique 3D packing of **Y6** compared with other molecules and to obtain more effective intermolecular 3D packing. Thus, it is essential to have an accurate single-crystal structure for such an analysis. Beautiful cuboid shape dark purple crystals were grown by a slow solvent diffusion (see the Method section in the Supprorting Information online) and were used for X-ray diffraction. The related parameters of **CH17** X-ray data were listed in Table S2 and those of **Y6** were obtained from Ref. [35]. From an overall view in Figure 2a, a 3D molecular packing network can be formed by both **CH17** and **Y6**. However, **CH17** forms square-shaped voids with a side length of ~12.8 Å, much smaller than that of ~29.2×22.2 Å obtained by **Y6** with rectangle-shaped voids (Table 1). Importantly, with respect to that of **Y6**, the significantly extended central unit of **CH17** is much more involved in the 3D packing network, contributing to more effective molecular packing with a larger total packing energy of −324 kJ/mol for **CH17** single cyrstal than that of −298 kJ/mol for **Y6**. The values of total packing energy were obtained by the method described in detail in Note S1 (Supprorting Information online) [54,55]. Note that the more effective and stronger molecular packing of **CH17** in 3D networks could facilitate the formation of more efficient 3D charge transport channels, resulting in the large charge mobility shown below and potentially superior OSC performance [21].

Intrinsically, the significant difference in 3D molecular packing discussed above in the crystals of **CH17** and **Y6** should be derived from their molecular difference and diverse intermolecular packing modes. From the single-crystal X-ray data in Figures S7 and S8, **CH17** possesses five packing modes with over 80 kJ/mol of intermolecular potential [54,55], including one newly observed distinctive mode of dual "end unit to central unit" ("dual E/C" mode, Mode 5 in Figure 2d) packing and the other four similar modes to those of **Y6**. The four similar packing modes of **CH17** and **Y6** were shown in Figure 2b and have been made a detailed comparison. Among them, Mode 1 and Mode 2 are the molecular packing only involving the "end unit to end unit" ("E/E" mode) interaction, existing in both **CH17** and **Y6** crystals and also playing a dominant role in other high-performance A-D-A type acceptors like **ITIC** [31,32] and **F** series [33,34] and donor [56] molecules. Note that the extended end unit of **CH17** makes a more effective packing with the bridged thiophene unit in Mode 2, rendering a smaller π-π packing distance of 3.27 Å than that of 3.35 Å for **Y6** (Figure 2c). This renders Mode 2 of **CH17** has an enhanced intermolecular interaction with a larger intermolecular potential of −133.3 kJ/mol compared with that of −91.3 kJ/mol for **Y6**. The Mode 3 is actually a dual (two-

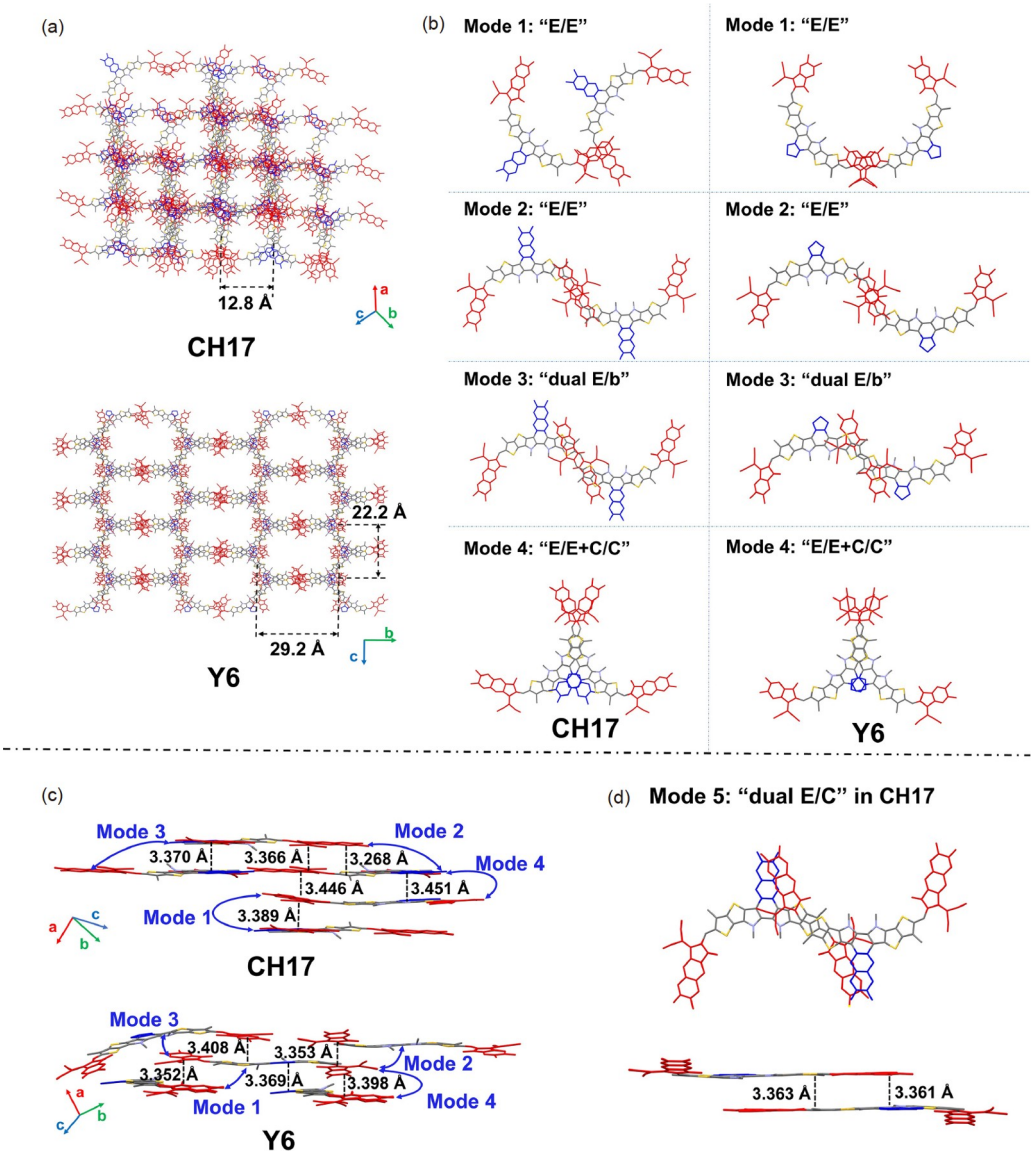

Figure 2 Single-crystal structures and intermolecular packing modes of **CH17** and **Y6**. (a) Single-crystal packing in view of the end-group stacking direction; (b) the four types of similar intermolecular packing modes of **CH17** and **Y6**; (c) π-π interlayer distances between acceptor molecular layers including four types of similar intermolecular packing modes; (d) the distinctive "dual E/C" packing mode and corresponding π-π interlayer distance of **CH17**. Note that all the end units were labeled with red, and the central units are labeled with blue. All the packing modes with UNI intermolecular potentials (>|80| kJ/mol) have been extracted (Figures S7 and S8) (color online).

way) packing mode between the end unit and bridged thiophene ("dual E/b" mode), which is also highly similar in both **CH17** and **Y6**. The Mode 4, which consists of both end/end unit and central/central unit ("E/E+C/C" mode) packing, was unique and first observed in **Y6** series and also plays probably the most important role for the 3D packing network in **Y6** series [21]. This "E/E+C/C" mode has an approximate facial overlap of ~50%, resulting in greatly enhanced intermolecular interaction in **Y6** crystal. Importantly, due to the multiple conjugation extension of central and end units of **CH17**, its "E/E+C/C" packing mode exhibits significantly larger overlap between the two neighboring packing molecules than that of **Y6**, leading to a much-enlarged intermolecular potential of −251.3 kJ/mol for **CH17** with respect to that of −198.6 kJ/mol for **Y6**. But the most intrigue packing mode in **CH17** is packing Mode 5 (Figure 2d), which has not been observed in **Y6** series before. In this mode, between the two neighboring packing molecules, the end unit **INIC-2F** in one molecule almost completely stacks on the central unit of another molecule, *e.g.*, a completely full and dual end unit to central unit packing mode ("dual E/C" mode) emerges and the bridged thiophene is fully involved in this packing mode. Note the stronger stacking between the neighboring molecules of this "dual E/C" mode

in **CH17** leads to a smaller π-π packing distance of 3.36 Å than that of 3.37–3.40 Å in the most effective packing mode (Mode 4) of **Y6** and also a large intermolecular potential of −231.7 kJ/mol for **CH17**. More importantly, it is clearly observed that the "dual E/C" mode plays an indispensable role in connecting adjacent unit cells of **CH17**, making its molecular packing successively along *c* axis by π-π staking, hence leading to a much more effective 3D packing network of **CH17** at solid state (Figure S9). Obviously, the newly observed and distinctive (Mode 5) and more effective intermolecular packing modes (such as Mode 4) of **CH17** should be caused by its multiple conjugation extension of both central and end units, which should be responsible for the enhanced charge transport, lower non-radiative recombination loss, and reduced E_{loss} for **CH17** based OSCs discussed below. It is important to note that such an effective and strongest "dual E/C" packing mode observed in **CH17** has not been reported before, as far as we know. In short, **CH17** exhibits a much stronger intermolecular coupling/packing among the neighboring molecules at solid state compared with the molecules of **Y6** series.

The enhanced molecular interaction with more and stronger packing modes of **CH17** should obviously originate from its different molecular structures and also configurations. As shown in Figure S10 and the X-ray data summaried in Table 1, both **CH17** and **Y6** demonstrate two configurations (**A** and **B**), and also there is a strong non-covalent S–O interaction [57] in the crystallographic networks. But, an unusual non-covalent S–N secondary interaction with a van der Waals distance of ~3.30 Å (the no-bonding S–N distance is ~3.50 Å [58]) between central unit and bridged thiophene is formed only in **CH17**. This non-covalently secondary interactions could also enhance the planarity and rigidity of **CH17** backbone with respect to that of **Y6**, which is also in favor of the observed strong intermolecular interaction and more ordered molecular packing and decreased electron reorganization energy discussed below. This would contribute to the lower energetic disorders in blend films of **CH17**, consistent with the observed reduced E_u below [18].

The multiple conjugation extension of **CH17** leads to markedly different intermolecular packing modes and better/stronger 3D molecular network, which will inevitably have a great influence on its charge transfer property. Therefore, the electron reorganization energy (λ), electron transfer integral (V_E), and hole transfer integral (V_H) of **CH17** were calculated to evaluate the charge transfer property [21,59]. As it can be expected, the enhanced molecular planarity and rigidity of **CH17** give rise to a smaller λ of 126 meV with respect to that of 148 meV for **Y6** (Table 1), rendering **CH17** as a potentially better charge transport material based on the Marcus charge-transfer theory [60]. Among all the five packing modes, the unique "dual E/C" molecular packing (Mode 5) in **CH17** possesses the most effective V_E of 76.0 meV and such a large V_E is well comparable with that of some most well-known *n*-type semiconductors such as perylene diimide (PDI) [61]. In sharp contrast, the largest V_E of **Y6** is obtained in Mode 4, being only 40.3 meV, much smaller than that of Mode 5 in **CH17**. Thus, the smaller λ and significantly enlarged electronic coupling of **CH17** with respect to those of **Y6** should afford a much better electron transport for **CH17** at solid state, which is confirmed by the measured higher electron mobility of 3.0×10^{-4} cm^2 V^{-1} S^{-1} for **CH17** comparing with that of 1.9×10^{-4} cm^2 V^{-1} S^{-1} for **Y6** (Table 1 and Figure S15). Interestingly, the largest V_H in Mode 5 of **CH17**

Table 1 Crystallographic and π-π interaction parameters of indicated acceptors

Compound	Void sizes (shape)	Packing modes	$d_{\pi\text{-}\pi}$ [b] (Å)	V_E [c] (meV)	V_H [c] (meV)	ConFigure [d]	$d_{S\text{-}N}$ [e] (Å)	μ_e/μ_h [f] (cm^2 V^{-1} s^{-1})
CH17	12.8 Å (square)	Mode 1 (E/E)	3.389	4.6	6.0	A	3.338/3.347	$3.0\times10^{-4}/1.9\times10^{-4}$
		Mode 2 (E/E)	3.268/3.366	32.1	8.1			
		Mode 3 (Dual E/b)	3.370	12.8	30.5			
		Mode 4 (E/E+C/C)	3.451/3.446	6.8	39.8	B	3.254/3.316	
		Mode 5 (Dual E/C)	3.361/3.363	76.0	110.7			
Y6 [a]	29.2×22.2 Å (rectangle)	Mode 1 (E/E)	3.352	9.5	9.7	A	3.622/3.600	$1.9\times10^{-4}/1.6\times10^{-4}$
		Mode 2 (E/E)	3.353	34.5	9.9			
		Mode 3 (Dual E/b)	3.408	10.3	81.4	B	3.581/3.566	
		Mode 4 (E/E+C/C)	3.369/3.398	40.3	32.0			

a) Crystal structure of **Y6** was obtained from previously reported work [35]. b) $d_{\pi\text{-}\pi}$ is the π-π interlayer distance including main types of intermolecular packing modes of **CH17** and **Y6**, which is consistent with that of Figure 2c. c) V_E is the electron transfer integral and V_H is the hole transfer integral of corresponding packing modes. The detailed calculation methods were described in Note S1. d) ConFigure represents configurations in crystals of **CH17** and **Y6**. e) $d_{S\text{-}N}$ represents the distance between S atom in bridged thiophene and N atom in central unit for two differrent configurations (A and B) of **CH17** and **Y6**. The S–N distances were also marked in Figure S10. f) Electron and hole mobility in optimized neat films of **CH17** and **Y6** were measured by space-charge-limited current (SCLC) method.

also reaches 110.7 meV, much larger than that of **Y6** (81.4 meV). This is consistent with the higher hole mobility of 1.9×10^{-4} cm^2 V^{-1} S^{-1} for **CH17** comparing with that of 1.6×10^{-4} cm^2 V^{-1} S^{-1} for **Y6**. This better 3D hole transport network of acceptor should be favorable for more effective hole transfer between donor and acceptor regardless of the acceptor molecular orientation at the donor/acceptor interfaces and further suppressed E_{loss} (discussed below) [21]. In brief, the both large and comparable V_E and V_H of the new and strongest "dual E/C" packing mode in **CH17** enables the formation of a more effective ambipolar transport network than that of **Y6**, indicating the conjugation extension of both central and end units is vital of importance in improving the charge transport in films.

2.3 Photovoltaic performance

To investigate the influence of the optimized 3D molecular packing network on device performance, **CH17** based OSCs with a conventional architecture of ITO glass/PEDOT:PSS/active layer/PDINO/Ag (ITO, indium tin oxide; PEDOT:PSS, poly(3,4-ethylenedioxythiophene):poly(4-styrenesulfonate); PDINO, 2,9-bis[3-(dimethyloxidoamino)propyl]anthra[2,1,9-def:6,5,10-d'e'f']diisoquinoline-1,3,8,10(2H,9H)-tetrone) (Figure 3a) were fabricated and have a compared study with **Y6** under the same conditions. Considering its matching energy levels and complementary absorption, a well-known polymeric donor **PM6** [53] (Figure S11) was selected to blend with **CH17** to afford the resulting active layer. The optimization of OSCs and the detailed photovoltaic parameters were summarized in Tables S3–S7. The optimal current density-voltage (*J*-*V*) curves of champion OSCs based on **CH17** and **Y6** were recorded in Figure 3b, demonstrating an improved PCE of 17.84% with respect to that of 16.27% for **Y6** based one.

In detail, the comparative and slightly improved J_{sc} of 26.19 mA cm^{-2} for **CH17** than that of 25.91 mA cm^{-2} for **Y6** based OSCs, respectively, are consistent with the similar absorption of their blend films (Figure S12), which also agrees well with the integrated J_{sc} of 25.39 and 25.27 mA cm^{-2} for **CH17** and **Y6**, respectively (Figure 3c and Table 2). Meanwhile, simultaneously improved V_{oc} of 0.883 V and FF of 77.2% have been obviously observed by **CH17** based OSCs compared with V_{oc} of 0.852 V and FF of 73.7% for those of **Y6**. Given that the almost identical E_g^{onset} and HOMO/LUMO for **CH17** and **Y6**, the enlarged V_{oc} and a smaller E_{loss} of **CH17** based OSCs caught our surprise, which will be discussed in details below. Figure 3d displays the efficiency distribution histogram for 15 independently measured OSCs, indicating the evidently higher average PCEs of **CH17** based OSCs than those of **Y6** counterparts. In order to improve the J_{sc} and further achieve a higher PCE for **CH17** based OSCs, a delicately selected acceptor **F-2F** (Figure S11) [33,34] with suitable energy levels and strong absorption in 660–810 nm region (Figure S13), was applied as a third component in **PM6**:**CH17** blends. As a consequence, the ternary OSCs using **PM6**:**CH17**:**F-2F** blends as active layers render an excellent PCE of 18.13% along with the fully upgraded V_{oc} of 0.889 V, J_{sc} of 26.6 mA cm^{-2}, and FF of 76.6% when comparing with **PM6**:**Y6** based OSCs. Importantly, it should be noted that the high V_{oc} of 0.889 V is rarely achieved in OSCs with PCE >18% [8–10].

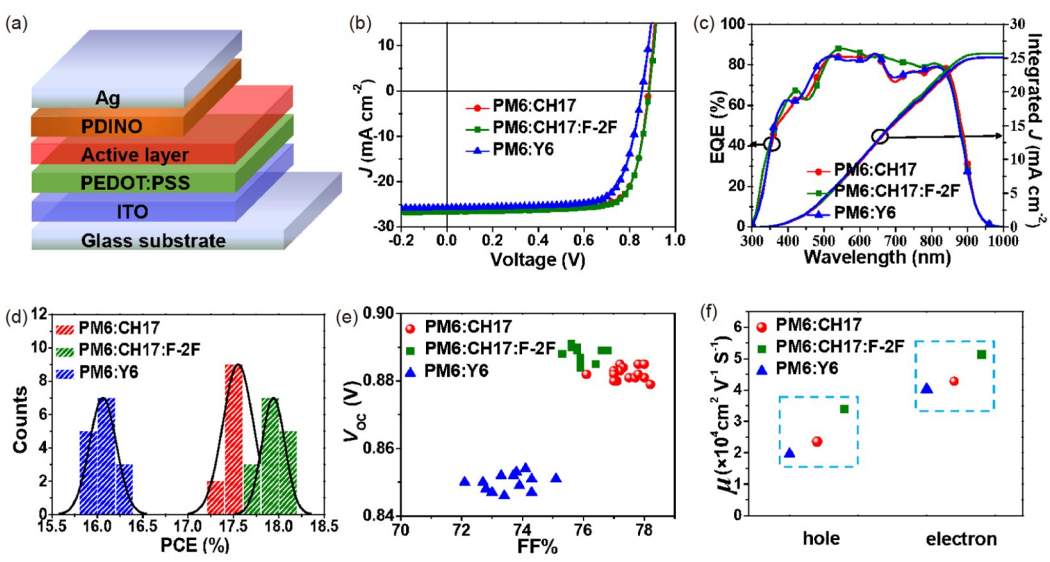

Figure 3 Photovoltaic performance of optimized **PM6**:**CH17**, **PM6**:**CH17**:**F-2F**, and **PM6**:**Y6**. (a) Device architecture of OSCs. (b) *J*-*V* curves and (c) EQE curves of the devices based on optimized **PM6**:**CH17**, **PM6**:**CH17**:**F-2F** and **PM6**:**Y6**. (d) Histogram of the efficiency measurements of **CH17**-based and **Y6**-based OSCs, fitted with Gaussian distributions (solid lines). (e) V_{oc} *versus* FF of **CH17**-based and **Y6**-based 15 independently measured OSCs (The corresponding device characteristics are given in Tables S5–S7). (f) Hole and electron mobilities of **PM6**:**CH17**, **PM6**:**CH17**:**F-2F** and **PM6**:**Y6** blends by SCLC measurements (color online).

The statistics for remarkable improvement of V_{oc}, FF and also comparative and slightly improved J_{sc} of **CH17** based OSCs than that of **Y6** could be intuitively observed from Figure 3e and Figure S14.

2.4 Charge transport, charge recombination and exciton dissociation

As we discussed above, more effective 3D transport networks have been observed in **CH17** crystal due to the multiple conjugation extension with respect to **Y6**. This will also influence the charge transport, charge recombination, and exciton dissociation of blend films and be further responsible for the improved photovoltaic performances and reduced E_{loss} of **CH17** based OSCs. As shown in Figure 3f, Table 3, and Figure S15, the estimated electron/hole mobilities (μ_e/μ_h) of **PM6**:**CH17**, **PM6**:**CH17**:**F-2F**, and **PM6**:**Y6** blend films were $4.3\times10^{-4}/2.4\times10^{-4}$, $5.1\times10^{-4}/3.4\times10^{-4}$, and $4.0\times10^{-4}/2.0\times10^{-4}$ cm^2 V^{-1} s^{-1}, with corresponding to μ_e/μ_h ratios of 1.8, 1.5 and 2.0, respectively. The higher and more balanced μ_e/μ_h ratios for **CH17**-based blended films are beneficial for the efficient charge transport and better FFs of resulting OSCs. In addition, **CH17** based OSC displays similar but slightly better exciton dissociation and charge recombination processes with respect to those of **Y6** based one, which is indicated by the similar J_{ph}/J_{sat} [62], α [63] and $S/(kT/q)$ [64] for **PM6**:**CH17**, **PM6**:**CH17**:**F-2F**, and **PM6**:**Y6** devices, respectively (Figures S16–S18).

2.5 Morphology analysis

Regarding the morphology in the active layer, the first question is whether the main molecular 3D packing modes of **CH17** in single crystals are kept in the blend films, which can be concluded by the comparison of the X-ray and other morphology results of **CH17** single crystal and its blend films. Considering that molecular packings in single crystals and spin-coating films might have some differences, some main sharp scattering peaks to determine the molecular packing orientation were extracted. As displayed in Figure S19, there are strong peaks of 0.32, 0.39, and 1.81 Å^{-1} observed in X-ray diffraction pattern generated from single crystal structure of **CH17**, corresponding to the packing distances of 19.89, 16.13, and 3.47 Å, respectively. This matches well with the grazing-incidence wide-angle X-ray scattering (GIWAXS) data in blend films, indicating that the packing modes of **CH17** in its single crystal are largely preserved in the spin-coated films (Figure S20 and Table S8), which is the case for **Y6** too [21]. Note that a favorable face-on orientation of molecular packing has also been kept by **CH17** after multiple conjugation extension, which should also be in favor of the efficient charge transport in blend films [9].

The multiple conjugation extension on **CH17** will inevitably result in the variation of microscopic morphology of the active layer, which plays a dominant role in the photovoltaic performance. Therefore, atomic force microscopy (AFM) was performed to unveil the morphology change at a level of nanoscale, and the obtained images are shown in Figure 4. The clearly formed nanofibers in **CH17** based blends should be reasonably attributed to the distinctive and more effective molecular packing of **CH17** with respect to that of **Y6**. Note that bundle-like structures of **CH17** based blends are formed by the aggregation of nanofibers to generate more free charge carriers, reduce charge recombination, facilitate charge transport, thus improving J_{sc} and FF for

Table 2 Summary of device parameters of the optimized OSCs [a)]

Active layer	V_{oc} (V)	J_{sc} (mA cm^{-2})	Calc. J_{sc} [b)] (mA cm^{-2})	FF (%)	PCE (%)
PM6:**CH17**	0.883 (0.882±0.002)	26.19 (25.71 ± 0.17)	25.39	77.2 (77.4 ± 0.4)	17.84 (17.55±0.13)
PM6:**CH17**:**F-2F**	0.889 (0.888±0.002)	26.62 (26.53±0.14)	26.01	76.6 (76.2±0.4)	18.13 (17.94±0.11)
PM6:**Y6**	0.852 (0.851±0.002)	25.91 (25.64± 0.27)	25.27	73.7 (73.6±0.6)	16.27 (16.06±0.12)

a) Optimal and statistical results are listed outside of parentheses and in parentheses, respectively. The average parameters were calculated from 15 independent devices. b) Current densities calculated from EQE curves.

Table 3 Charge carrier transport parameters of the optimized **PM6**:**Y6**, **PM6**:**CH17**, and **PM6**:**CH17**:**F-2F** BHJ blends and devices

Blend films	μ_e [a)] (10^{-4} cm^2 V^{-1} s^{-1})	μ_h [a)] (10^{-4} cm^2 V^{-1} s^{-1})	μ_e/μ_h	J_{ph}/J_{sat} [b)] (%)	α [c)] (%)	$S/(kT/q)$ [d)]
PM6:**CH17**	4.3	2.4	1.8	97.08	98.26	1.18
PM6:**CH17**:**F-2F**	5.2	3.4	1.5	97.16	98.30	1.17
PM6:**Y6**	4.0	2.0	2.0	96.84	98.25	1.21

a) μ_e and μ_h are electron and hole mobilities of optimized **PM6**:**CH17**, **PM6**:**CH17**:**F-2F**, and **PM6**:**Y6** blends by SCLC measurements. b) J_{ph}/J_{sat} was obtained from J_{ph}-V_{eff} pots of optimized OSCs. c) α was obtained from pots of dependence of current density (J_{sc}) on P_{light} of optimized OSCs. d) S is the slop of V_{oc} *versus* the natural logarithm of P_{light} obtained from plots of dependence of V_{oc} on P_{light} of optimized OSCs (Figure 3f and Figures S15–S18).

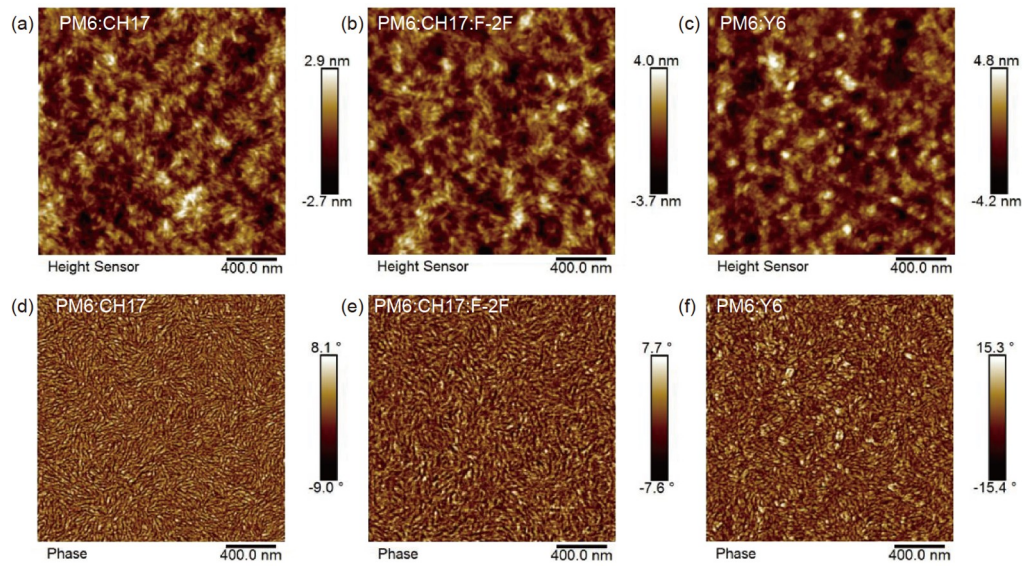

Figure 4 Morphology characterization of blend films. (a, d) AFM height and phase images of optimized **PM6**:**CH17** film; (b, e) AFM height and phase images of optimized **PM6**:**CH17**:**F-2F** film; (c, f) AFM height and phase images of optimized **PM6**:**Y6** film. The root-mean-square roughness values are 0.89, 0.98, and 1.25 nm for optimized **PM6**:**CH17**, **PM6**:**CH17**:**F-2F**, and **PM6**:**Y6** films, respectively (color online).

CH17 based OSCs [65], demonstrating the vital roles of conjugation extension of both central and end units in morphology engineering. Furthermore, the overall morphological characteristics suggested by the images have been fully confirmed by corresponding TEM images (Figure S21).

2.6 Energy loss analysis of OSCs

How to suppress E_{loss} and further maximize V_{oc} by rational molecular design is the key point of efficient OSCs but still confronts a great challenge [36]. Given that **CH17** possesses the almost identical E_g^{onset} (but with even red-shifted solution absorption shown in Figure S1) with **Y6**, it is naturally logical to draw the connection between the multiple conjugation extension in **CH17** with the significantly larger V_{oc} and thus reduced E_{loss} of its OSCs. In general, E_{loss} in OSCs can be regarded originating from three parts: ΔE_{CT}, ΔV_r, and ΔV_{nr} [15]. Among them, ΔE_{CT} represents the energetic difference between the singlet excited state (also named local exciton (LE) state) and charge transfer (CT) state, which is essential for the exciton separation, whereas leading to the first part of unwanted voltage loss. ΔV_r is the voltage loss induced by inevitable radiative recombination and hard to be depressed [66]. ΔV_{nr} could be described as the voltage loss caused by the most-concerned non-radiative recombination, and thus its suppression through molecular and morphology engineering is the most approached but challenging to further improve the V_{oc} and PCEs of OSCs [20].

The total E_{loss} of OSCs can be determined by the following equation: $E_{loss}=E_g-eV_{oc}$, where E_g is estimated by the cross-point of normalized absorption and emission spectra of neat film [67,68], being 1.38 eV for **PM6**:**CH17**, **PM6**:**CH17**:**F-2F**, and **PM6**:**Y6**, respectively (Figure S22). To further verify these data, E_g of blended films have also been evaluated through the derivatives of EQE spectra and is very closed to cross-point of normalized absorption and emission spectra of neat film (Figure S23). Thus, the total E_{loss} of **PM6**:**CH17** and **PM6**:**CH17**:**F-2F** based OSCs are as low as 0.50 and 0.49 eV, respectively. These values are much smaller than that of 0.53 eV for **PM6**:**Y6**, ranking **CH17** based OSCs among the smallest E_{loss} systems, especially in high PCE systems [8–10]. Note that the absorption of CT states contributes to the low energy part of EQE spectra, and thus E_{CT} of three OSCs can be estimated by fitting the corresponding highly sensitive EQEs (sEQE) and electroluminescence spectra (EL) (Figure 5a–c and Figure S24) [15]. As a result, the E_{CT} values of OSCs based on **PM6**:**CH17**, **PM6**:**CH17**:**F-2F**, and **PM6**:**Y6** are determined to be 1.34, 1.36, and 1.33 eV, respectively. With such high CT states close to its LE state (E_g), the potential hybridization of LE and CT states caused by electronic couplings ($t_{LE\text{-}CT}$) should be taken into consideration based on recently developed three-state model (Figure 5d) [22,69]. There are no clear sub-bandgap CT-state features from both sEQE and EL measurements of **CH17** and **Y6** based devices [21], also implying the occurrence of hybridization of LE and CT states in both **CH17** and **Y6** blends and consisting with their small ΔE_{CT} shown in Table 4. With almost the same E_g, the higher E_{CT} of **CH17** blends compared with that of **Y6** renders more sufficient hybridization of CT state with LE state and probably also a weakened electron-vibration coupling between the lowest energy CT state and the highest vibrational ground (G) state [70], thus enlarges the radiative rate of CT state *via* an intensity borrowing mechanism [23] or the energetically

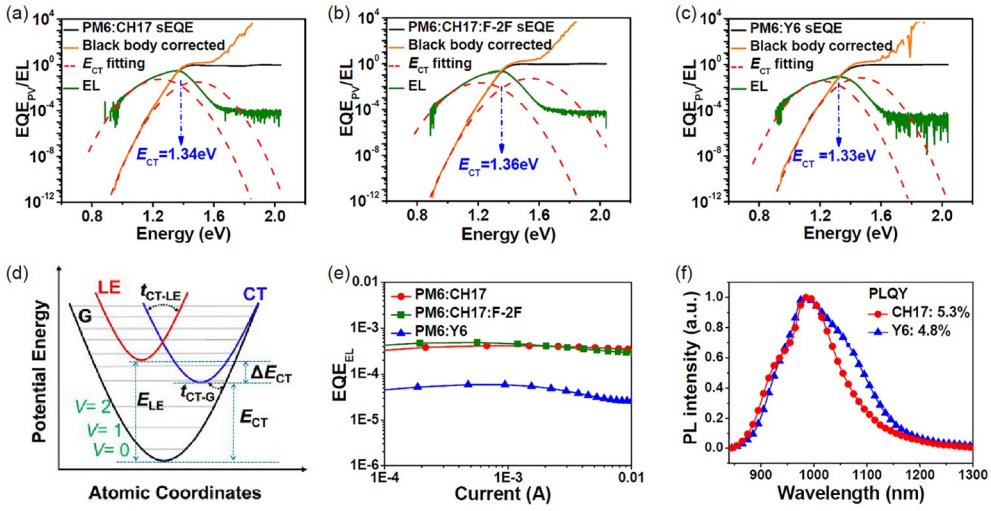

Figure 5 Energy loss analysis in **PM6**:NFAs based solar cells. (a–c) Sensitive external quantum efficiency (sEQE) spectra and the fitting results for the relevant devices. sEQE, black lines; electroluminescence spectra (EL, green lines); sEQE and EL fitting results (red dashed lines), and sEQE spectra were calculated using the reciprocal relations of EL (orange lines). (d) A schematic diagram of the potential energy curves for the ground (G), charge transfer (CT), and local exciton (LE) diabatic states. ΔE_{CT} denotes the relaxed excitation energy of the LE and CT states, whereas $t_{CT\text{-}G}$ and $t_{LE\text{-}CT}$ represent the electronic couplings of the CT state with the G and LE states, respectively. (e) EQE$_{EL}$ spectra of the **PM6**:NFA based OSCs. (f) Photoluminescence spectra of the **CH17** and **Y6** films excited at 825 nm together with their quantum efficiencies (color online).

Table 4 Total energy loss values and different contributions in solar cells

Active layer	V_{oc} (V)	E_g [a)] (eV)	E_{CT} [b)] (eV)	ΔE_{CT} [c)] (eV)	ΔV_r (V)	ΔV_{nr} [d)] (V)	E_{loss} (eV)	EQE$_{EL}$ ($\times 10^{-4}$)	E_u [e)] (meV)
PM6:**CH17**	0.88	1.38	1.34	0.04	0.27	0.19	0.50	4.17	20.8
PM6:**CH17**:**F-2F**	0.89	1.38	1.36	0.02	0.28	0.19	0.49	4.71	21.5
PM6:**Y6**	0.85	1.38	1.33	0.05	0.24	0.24	0.53	0.60	23.1

a) E_g is estimated by the cross-point of normalized absorption and emission spectra of neat film. b) E_{CT} was obtained by fittings (red dashed curve in Figure 5) to the low energy part of the sEQE spectra and EL spectra. c) ΔE_{CT} is calculated by the following equation: $\Delta E_{CT}=E_g-E_{CT}$. d) ΔV_{nr} is the voltage loss by non-radiative recombination and is calculated by the following equation: $\Delta V_{nr}=(kT/q)\ln(1/\text{EQE}_{EL})$ [70]. e) Urbach energies was estimated *via* the fittings sEQE onset (Figure S25).

possible back transition from CT state to LE state. Considering possible fitting error of CT state in the system without obvious CT-state features [71–73], the more sufficient hybridization of CT state with LE state could also be indicated by the larger $t_{LE\text{-}CT}$ of **CH17** compared with that of **Y6** ($t_{LE\text{-}CT}$: 25 meV for **PM6**:**CH17** and 12 meV for **PM6**:**Y6**, respectively, based on three-state model [22]). These characteristics should allow the CT state to undergo more effectively radiative recombination *via* the hybridization with the emissive LE state as well as importantly the strong emission of the LE state due to its larger thermal population, which could lead to a higher EQE$_{EL}$ of 4.17×10^{-4} for **CH17** based device compared with that of 5.98×10^{-5} for **Y6** based one (Figure 5e), corresponding to a significantly smaller ΔV_{nr} of ~0.19 V for **CH17** based OSCs comparing to that of 0.24 V for **Y6** based one. Note such about a one-order increase of EQE$_{EL}$ is very significant [22]. As we can see clearly from the Figure S24, a narrower EL emission width of **CH17**-based film with low reorganization energies is also convinced evidence for the much-suppressed V_{nr} [74]. As shown in Figure 5f, the smaller ΔV_{nr} of **CH17** is also consistent with its higher photoluminescence quantum yield (PLQY) of 5.3% compared with that of 4.8% for **Y6** in the pristine material. Note that the PLQY of the pristine material components has been proved to define the limit of ΔV_{nr} in organic solar cells when ΔE_{CT} is small (<0.2 eV) [22,69].

In addition, we also analyzed the E_u in the active layers, which is usually described as the width of the tail of the electronic density of states (DOS) for photoactive layers [75] and reflects the degree of overall energy disorder [76]. Herein, much lower E_u values of 20.8 and 21.5 meV for **PM6**:**CH17** and **PM6**:**CH17**:**F-2F**, compared with that of 23.1 meV for **PM6**:**Y6** (Figure S25), have been observed. As a rule of thumb, a smaller E_u for **CH17** based OSCs, which should be caused by its more ordered molecular packing [77], indicates a lower energetic disorder and hence contributes to its reduced charge recombination and lower non-radiative recombination loss [18].

To summarize, **CH17** based OSC possesses almost identical E_g but significantly suppressed ΔV_{nr} and E_{loss} compared with those of **Y6** based one. Based on all the above molecular structure and morphology analysis of single crystal, GI-

WAXS, AFM, TEM *etc*. for **CH17** and its blend used in OSCs, and together with the device photodynamic and performance studies, some important conclusions originating from the vital role of multiple conjugation extension should be noted: (1) at a molecular level, the extended conjugation enhances the molecular rigidity and planarity with reduced reorganization energy; (2) the more effective/stronger intermolecular 3D packing network, particularly the unique and previously unobserved "dual E/C" (Mode 5 in Figure 2d) packing mode with the largest intermolecular electron and hole transfer integrals of 76.0 and 110.7 meV, respectively in **CH17**, affords a better 3D charge transport channel for both electron and hole with respect to that of **Y6**; (3) the increased CT state leads to a stronger hybridization between CT and LE states, which greatly enhances the radiative recombination and simultaneously suppress the non-radiative recombination process; (4) the largely reduced energetic disorder of **CH17** as indicated by smaller E_u due to more ordered crystals packing is also reducing the non-radiative recombination.

All these combined together make the radiative recombination more efficient [21] supported by the higher PLQY, and thus mitigate the non-radiative recombination loss indicated by the higher EQE_{EL}, to produce a stronger 3D network in both single crystal and blend films of CH17 with remarkably lower E_{loss} and higher V_{oc} in its OSC devices, which finally leads to higher device performance compared with that of **Y6**.

3 Conclusion

A novel A-D-A type acceptor **CH17** has been designed and synthesized by conjugation extension in both directions of central and end units on the basis of a typical **Y6** molecule to engineer molecular packing and tackle the large E_{loss} of OSCs for better performance. The large conjugation extension of **CH17** affords indeed a much more optimized and stronger 3D molecular network and also with an unreported strong intermolecular packing mode of "dual E/C", leading to better charge transport, better radiative recombination with higher luminescence efficiency and reduced non-radiative recombination loss, and much decreased energetic disorder of blend films comparing with those of **Y6**. As a result, an excellent PCE of 18.13%, along with a remarkably lower E_{loss} of 0.49 eV (ΔV_{nr}<0.2 V) for **CH17** based ternary devices (a PCE of 17.84% with E_{loss} of 0.50 eV for **CH17** based binary devices) is achieved. These results indicate that there is still large room for addressing the large E_{loss} *via* morphology engineering to break through the PCE bottleneck of OSCs, through dedicated molecule design, such as multiple conjugation extension used in this work, and will stimulate further extensive explorations for NFAs systems with the feature of low non-radiative recombination loss.

Acknowledgements This work was supported by the National Natural Sciences Foundation of China (21935007, 52025033, 51873089), MoST of China (2019YFA0705900), Tianjin city (20JCZDJC00740), 111 Project (B12015), and the Opening Project of State Key Laboratory of Luminescent Materials and Devices (SCUT, 2021-skllmd-09). We also acknowledge the GIWAXS measurements provided by Prof Zhixiang Wei at the National Center for Nanoscience and Technology, CAS, Beijing, China. All the theoretical calculations were performed on National Supercomputer Center in Guangzhou.

Conflict of interest The authors declare no conflict of interest.

Supporting information The supporting information is available online at http://chem.scichina.com and http://link.springer.com/journal/11426. The supporting materials are published as submitted, without typesetting or editing. The responsibility for scientific accuracy and content remains entirely with the authors.

1 Gillett AJ, Privitera A, Dilmurat R, Karki A, Qian D, Pershin A, Londi G, Myers WK, Lee J, Yuan J, Ko SJ, Riede MK, Gao F, Bazan GC, Rao A, Nguyen TQ, Beljonne D, Friend RH. *Nature*, 2021, 597: 666–671
2 Song W, Liu Y, Fanady B, Han Y, Xie L, Chen Z, Yu K, Peng X, Zhang X, Ge Z. *Nano Energy*, 2021, 86: 106044
3 Hu Z, Wang J, Ma X, Gao J, Xu C, Yang K, Wang Z, Zhang J, Zhang F. *Nano Energy*, 2020, 78: 105376
4 Sun C, Qin S, Wang R, Chen S, Pan F, Qiu B, Shang Z, Meng L, Zhang C, Xiao M, Yang C, Li Y. *J Am Chem Soc*, 2020, 142: 1465–1474
5 Jing J, Dong S, Zhang K, Xie B, Zhang J, Song Y, Huang F. *Nano Energy*, 2022, 93: 106814
6 Chen Y, Wan X, Long G. *Acc Chem Res*, 2013, 46: 2645–2655
7 Wan X, Li C, Zhang M, Chen Y. *Chem Soc Rev*, 2020, 49: 2828–2842
8 Cui Y, Xu Y, Yao H, Bi P, Hong L, Zhang J, Zu Y, Zhang T, Qin J, Ren J, Chen Z, He C, Hao X, Wei Z, Hou J. *Adv Mater*, 2021, 33: 2102420
9 Li C, Zhou J, Song J, Xu J, Zhang H, Zhang X, Guo J, Zhu L, Wei D, Han G, Min J, Zhang Y, Xie Z, Yi Y, Yan H, Gao F, Liu F, Sun Y. *Nat Energy*, 2021, 6: 605–613
10 Bao S, Yang H, Fan H, Zhang J, Wei Z, Cui C, Li Y. *Adv Mater*, 2021, 33: 2105301
11 Jena AK, Kulkarni A, Miyasaka T. *Chem Rev*, 2019, 119: 3036–3103
12 Yoshikawa K, Kawasaki H, Yoshida W, Irie T, Konishi K, Nakano K, Uto T, Adachi D, Kanematsu M, Uzu H, Yamamoto K. *Nat Energy*, 2017, 2: 17032
13 Wu J, Cha H, Du T, Dong Y, Xu W, Lin CT, Durrant JR. *Adv Mater*, 2022, 34: 2101833
14 Chen S, Tsang SW, Lai TH, Reynolds JR, So F. *Adv Mater*, 2014, 26: 6125–6131
15 Liu H, Li M, Wu H, Wang J, Ma Z, Tang Z. *J Mater Chem A*, 2021, 9: 19770–19777
16 Jeong M, Choi IW, Go EM, Cho Y, Kim M, Lee B, Jeong S, Jo Y, Choi HW, Lee J, Bae JH, Kwak SK, Kim DS, Yang C. *Science*, 2020, 369: 1615–1620
17 Meng L, Zhang Y, Wan X, Li C, Zhang X, Wang Y, Ke X, Xiao Z, Ding L, Xia R, Yip HL, Cao Y, Chen Y. *Science*, 2018, 361: 1094–1098
18 Liu S, Yuan J, Deng W, Luo M, Xie Y, Liang Q, Zou Y, He Z, Wu H, Cao Y. *Nat Photonics*, 2020, 14: 300–305
19 Hou J, Inganäs O, Friend RH, Gao F. *Nat Mater*, 2018, 17: 119–128
20 An N, Cai Y, Wu H, Tang A, Zhang K, Hao X, Ma Z, Guo Q, Ryu HS, Woo HY, Sun Y, Zhou E. *Adv Mater*, 2020, 32: 2002122
21 Zhang G, Chen XK, Xiao J, Chow PCY, Ren M, Kupgan G, Jiao X,

Chan CCS, Du X, Xia R, Chen Z, Yuan J, Zhang Y, Zhang S, Liu Y, Zou Y, Yan H, Wong KS, Coropceanu V, Li N, Brabec CJ, Bredas JL, Yip HL, Cao Y. *Nat Commun*, 2020, 11: 3943
22 Chen XK, Qian D, Wang Y, Kirchartz T, Tress W, Yao H, Yuan J, Hülsbeck M, Zhang M, Zou Y, Sun Y, Li Y, Hou J, Inganäs O, Coropceanu V, Bredas JL, Gao F. *Nat Energy*, 2021, 6: 799–806
23 Qian D, Zheng Z, Yao H, Tress W, Hopper TR, Chen S, Li S, Liu J, Chen S, Zhang J, Liu XK, Gao B, Ouyang L, Jin Y, Pozina G, Buyanova IA, Chen WM, Inganäs O, Coropceanu V, Bredas JL, Yan H, Hou J, Zhang F, Bakulin AA, Gao F. *Nat Mater*, 2018, 17: 703–709
24 Fei Z, Eisner FD, Jiao X, Azzouzi M, Röhr JA, Han Y, Shahid M, Chesman ASR, Easton CD, McNeill CR, Anthopoulos TD, Nelson J, Heeney M. *Adv Mater*, 2018, 30: 1705209
25 Gao W, Zhang M, Liu T, Ming R, An Q, Wu K, Xie D, Luo Z, Zhong C, Liu F, Zhang F, Yan H, Yang C. *Adv Mater*, 2018, 30: 1800052
26 Huang H, Guo Q, Feng S, Zhang C', Bi Z, Xue W, Yang J, Song J, Li C, Xu X, Tang Z, Ma W, Bo Z. *Nat Commun*, 2019, 10: 3038
27 Yuan J, Zhang Y, Zhou L, Zhang G, Yip HL, Lau TK, Lu X, Zhu C, Peng H, Johnson PA, Leclerc M, Cao Y, Ulanski J, Li Y, Zou Y. *Joule*, 2019, 3: 1140–1151
28 Zhu L, Zhang M, Zhou G, Hao T, Xu J, Wang J, Qiu C, Prine N, Ali J, Feng W, Gu X, Ma Z, Tang Z, Zhu H, Ying L, Zhang Y, Liu F. *Adv Energy Mater*, 2020, 10: 1904234
29 Guo X, Fan Q, Wu J, Li G, Peng Z, Su W, Lin J, Hou L, Qin Y, Ade H, Ye L, Zhang M, Li Y. *Angew Chem Int Ed*, 2021, 60: 2322–2329
30 Wang R, Yuan J, Wang R, Han G, Huang T, Huang W, Xue J, Wang HC, Zhang C, Zhu C, Cheng P, Meng D, Yi Y, Wei KH, Zou Y, Yang Y. *Adv Mater*, 2019, 31: 1904215
31 Lin Y, Wang J, Zhang ZG, Bai H, Li Y, Zhu D, Zhan X. *Adv Mater*, 2015, 27: 1170–1174
32 Yao H, Cui Y, Yu R, Gao B, Zhang H, Hou J. *Angew Chem Int Ed*, 2017, 56: 3045–3049
33 Ke X, Meng L, Wan X, Li M, Sun Y, Guo Z, Wu S, Zhang H, Li C, Chen Y. *J Mater Chem A*, 2020, 8: 9726–9732
34 Qiu N, Zhang H, Wan X, Li C, Ke X, Feng H, Kan B, Zhang H, Zhang Q, Lu Y, Chen Y. *Adv Mater*, 2017, 29: 1604964
35 Zhu W, Spencer AP, Mukherjee S, Alzola JM, Sangwan VK, Amsterdam SH, Swick SM, Jones LO, Heiber MC, Herzing AA, Li G, Stern CL, DeLongchamp DM, Kohlstedt KL, Hersam MC, Schatz GC, Wasielewski MR, Chen LX, Facchetti A, Marks TJ. *J Am Chem Soc*, 2020, 142: 14532–14547
36 Cui Y, Yao H, Zhang J, Zhang T, Wang Y, Hong L, Xian K, Xu B, Zhang S, Peng J, Wei Z, Gao F, Hou J. *Nat Commun*, 2019, 10: 2515
37 Fan B, Lin F, Oh J, Fu H, Gao W, Fan Q, Zhu Z, Li WJ, Li N, Ying L, Huang F, Yang C, Jen AK. *Adv Energy Mater*, 2021, 11: 2101768
38 Li G, Zhang X, Jones LO, Alzola JM, Mukherjee S, Feng LW, Zhu W, Stern CL, Huang W, Yu J, Sangwan VK, DeLongchamp DM, Kohlstedt KL, Wasielewski MR, Hersam MC, Schatz GC, Facchetti A, Marks TJ. *J Am Chem Soc*, 2021, 143: 6123–6139
39 Li S, Li CZ, Shi M, Chen H. *ACS Energy Lett*, 2020, 5: 1554–1567
40 Li S, Zhan L, Yao N, Xia X, Chen Z, Yang W, He C, Zuo L, Shi M, Zhu H, Lu X, Zhang F, Chen H. *Nat Commun*, 2021, 12: 4627
41 Chang Y, Zhang J, Chen Y, Chai G, Xu X, Yu L, Ma R, Yu H, Liu T, Liu P, Peng Q, Yan H. *Adv Energy Mater*, 2021, 11: 2100079
42 Lin F, Jiang K, Kaminsky W, Zhu Z, Jen AKY. *J Am Chem Soc*, 2020, 142: 15246–15251
43 Luo Z, Sun R, Zhong C, Liu T, Zhang G, Zou Y, Jiao X, Min J, Yang C. *Sci China Chem*, 2020, 63: 361–369
44 Mo D, Chen H, Zhou J, Tang N, Han L, Zhu Y, Chao P, Lai H, Xie Z, He F. *J Mater Chem A*, 2020, 8: 8903–8912
45 Qin R, Wang D, Zhou G, Yu ZP, Li S, Li Y, Liu ZX, Zhu H, Shi M, Lu X, Li CZ, Chen H. *J Mater Chem A*, 2019, 7: 27632–27639
46 Wang L, Guo C, Zhang X, Cheng S, Li D, Cai J, Chen C, Fu Y, Zhou J, Qin H, Liu D, Wang T. *Chem Mater*, 2021, 33: 8854–8862
47 Yang C, An Q, Bai HR, Zhi HF, Ryu HS, Mahmood A, Zhao X, Zhang S, Woo HY, Wang JL. *Angew Chem Intl Edit*, 2021, 60: 19241–19252
48 Liu T, Zhang Y, Shao Y, Ma R, Luo Z, Xiao Y, Yang T, Lu X, Yuan Z, Yan H, Chen Y, Li Y. *Adv Funct Mater*, 2020, 30: 2000456
49 Zhou Z, Liu W, Zhou G, Zhang M, Qian D, Zhang J, Chen S, Xu S, Yang C, Gao F, Zhu H, Liu F, Zhu X. *Adv Mater*, 2020, 32: 1906324
50 Zhu C, An K, Zhong W, Li Z, Qian Y, Su X, Ying L. *Chem Commun*, 2020, 56: 4700–4703
51 Feng H, Qiu N, Wang X, Wang Y, Kan B, Wan X, Zhang M, Xia A, Li C, Liu F, Zhang H, Chen Y. *Chem Mater*, 2017, 29: 7908–7917
52 Shi Y, Pan J, Yu J, Zhang J, Gao F, Lu K, Wei Z. *Sol RRL*, 2021, 5: 2100008
53 Qian D, Ye L, Zhang M, Liang Y, Li L, Huang Y, Guo X, Zhang S, Tan Z', Hou J. *Macromolecules*, 2012, 45: 9611–9617
54 Gavezzotti A, Filippini G. *J Phys Chem*, 1994, 98: 4831–4837
55 Gavezzotti A. *Acc Chem Res*, 1994, 27: 309–314
56 Sun K, Xiao Z, Lu S, Zajaczkowski W, Pisula W, Hanssen E, White JM, Williamson RM, Subbiah J, Ouyang J, Holmes AB, Wong WWH, Jones DJ. *Nat Commun*, 2015, 6: 6013
57 Liu Y, Zhang Z, Feng S, Li M, Wu L, Hou R, Xu X, Chen X, Bo Z. *J Am Chem Soc*, 2017, 139: 3356–3359
58 Politzer P, Murray JS. *Struct Chem*, 2021, 32: 623–629
59 Shuai Z, Geng H, Xu W, Liao Y, André JM. *Chem Soc Rev*, 2014, 43: 2662–2679
60 Marcus RA. *Angew Chem Int Ed*, 1993, 32: 1111–1121
61 Geng H, Peng Q, Wang L, Li H, Liao Y, Ma Z, Shuai Z. *Adv Mater*, 2012, 24: 3568–3572
62 Li G, Li D, Ma R, Liu T, Luo Z, Cui G, Tong L, Zhang M, Wang Z, Liu F, Xu L, Yan H, Tang B. *J Mater Chem A*, 2020, 8: 5927–5935
63 Koster LJA, Kemerink M, Wienk MM, Maturová K, Janssen RAJ. *Adv Mater*, 2011, 23: 1670–1674
64 Kyaw AKK, Wang DH, Gupta V, Leong WL, Ke L, Bazan GC, Heeger AJ. *ACS Nano*, 2013, 7: 4569–4577
65 Liu Q, Jiang Y, Jin K, Qin J, Xu J, Li W, Xiong J, Liu J, Xiao Z, Sun K, Yang S, Zhang X, Ding L. *Sci Bull*, 2020, 65: 272–275
66 Miller OD, Yablonovitch E, Kurtz SR. *IEEE J Photovol*, 2012, 2: 303–311
67 Wang Y, Qian D, Cui Y, Zhang H, Hou J, Vandewal K, Kirchartz T, Gao F. *Adv Energy Mater*, 2018, 8: 1801352
68 Vandewal K, Benduhn J, Nikolis VC. *Sustain Energy Fuels*, 2018, 2: 538–544
69 Eisner FD, Azzouzi M, Fei Z, Hou X, Anthopoulos TD, Dennis TJS, Heeney M, Nelson J. *J Am Chem Soc*, 2019, 141: 6362–6374
70 Benduhn J, Tvingstedt K, Piersimoni F, Ullbrich S, Fan Y, Tropiano M, McGarry KA, Zeika O, Riede MK, Douglas CJ, Barlow S, Marder SR, Neher D, Spoltore D, Vandewal K. *Nat Energy*, 2017, 2: 17053
71 Armin A, Zarrabi N, Sandberg OJ, Kaiser C, Zeiske S, Li W, Meredith P. *Adv Energy Mater*, 2020, 10: 2001828
72 List M, Sarkar T, Perkhun P, Ackermann J, Luo C, Würfel U. *Nat Commun*, 2018, 9: 3631
73 Perdigón-Toro L, Phuong LQ, Zeiske S, Vandewal K, Armin A, Shoaee S, Neher D. *ACS Energy Lett*, 2021, 6: 557–564
74 Liu Q, Smeets S, Mertens S, Xia Y, Valencia A, D'Haen J, Maes W, Vandewal K. *Joule*, 2021, 5: 2365–2379
75 Garcia-Belmonte G, Boix PP, Bisquert J, Lenes M, Bolink HJ, La Rosa A, Filippone S, Martín N. *J Phys Chem Lett*, 2010, 1: 2566–2571
76 Urbach F. *Phys Rev*, 1953, 92: 1324
77 Zhang Z, Li Y, Cai G, Zhang Y, Lu X, Lin Y. *J Am Chem Soc*, 2020, 142: 18741–18745